

Article

# Preparation and Two-Photon Photoluminescence Properties of Organic Inorganic Hybrid Perovskites $(\text{C}_6\text{H}_5\text{CH}_2\text{NH}_3)_2\text{PbBr}_4$ and $(\text{C}_6\text{H}_5\text{CH}_2\text{NH}_3)_2\text{PbI}_4$

Shuai Liu, Fang Li \*, Xiaobo Han, Litu Xu, Fuqiang Yao and Yahui Liu

Laboratory of Optical Information and Technology, School of Optoelectronics and Energy, Wuhan Institute of Technology, Wuhan 430073, China; 15342251052@163.com (S.L.); hanxiaobo@wit.edu.cn (X.H.); 15871430579@163.com (L.X.); yfq15872268171@163.com (F.Y.); 13212799763@163.com (Y.L.)

\* Correspondence: lifang@wit.edu.cn or lifang\_wit@hotmail.com; Tel.: +86-027-8799-2024

Received: 13 October 2018; Accepted: 14 November 2018; Published: 19 November 2018



**Abstract:** Organic inorganic hybrid perovskites have potential applications in solar cells, electroluminescent devices and radiation detection because of their unique optoelectronic properties. In this paper, the perovskites  $(\text{C}_6\text{H}_5\text{CH}_2\text{NH}_3)_2\text{PbBr}_4$  and  $(\text{C}_6\text{H}_5\text{CH}_2\text{NH}_3)_2\text{PbI}_4$  were synthesized by solvent evaporation. The crystal structure, morphology, absorption spectrum, laser power dependence of the photoluminescence (PL) intensity and lifetime were studied. The results showed that the perovskites  $(\text{C}_6\text{H}_5\text{CH}_2\text{NH}_3)_2\text{PbBr}_4$  and  $(\text{C}_6\text{H}_5\text{CH}_2\text{NH}_3)_2\text{PbI}_4$  display a layered stacking structure of organic and inorganic components. The absorption peaks are located at 392 nm (3.16 eV) and 516 nm (2.40 eV), respectively. It was observed that the PL intensity and photoluminescence quantum yield (PLQY) increases with increasing laser power, and that the PL lifetime decreases with increasing laser power, which is mainly due to the non-geminate recombination.

**Keywords:** perovskites; two-photon excitation; photoluminescence spectrum; photoluminescence lifetime

## 1. Introduction

In recent years, organic inorganic hybrid perovskites have received wide attention and investigation as the most competitive candidates in photovoltaic field development. Organic inorganic hybrid perovskites are a new subclass of material self-assembled at the molecular scale from organic and inorganic components [1–3]. The crystal structure of a perovskite can be described with the chemical formula  $\text{ABX}_3$ , in which A-sites are the organic ammonium cations, B-sites are the inorganic metal cations, and X-sites are the halide anions. The B-site cation is six-coordinated by the X-site anion to form  $[\text{BX}_6]$  octahedrons, which are corner-sharing to constitute three-dimensional frameworks [4,5]. These compounds have multiple quantum well structures with alternating organic and inorganic layers [6]. In these compounds, the excitons possess larger binding energy due to quantum confinement effects, which displays excellent optical properties such as second harmonic generation, exciton absorption and emission [7–11]. These properties make organic inorganic hybrid perovskites great candidates for applications in solar cells [12], electroluminescent devices [13–15] and radiation detection [16].

The perovskite solar cells with all solid state structure can prevent the problems from the liquid electrolyte and exhibit high power conversion efficiency (PCE), displaying great potential in photovoltaic devices. In 2009, Miyasaka et al. [17] firstly studied the solar cells with the perovskite  $\text{CH}_3\text{NH}_3\text{PbI}_3$ , yielding a PCE of 3.8% due to the lower open voltage. In 2011, Zheng et al. [18] synthesized a series of the perovskites  $(\text{C}_6\text{H}_{13}\text{NH}_3)_2(\text{CH}_3\text{NH}_3)_{n-1}\text{Pb}_n\text{I}_{3n+1}$ , and investigated the effects

of the inorganic-sheet number on the crystal structure, bandgap energy, exciton binding energy and photoluminescent emission. In 2013, Stoumpos et al. [19] synthesized several perovskites  $\text{CH}_3\text{NH}_3\text{SnI}_3$ ,  $\text{HC}(\text{NH}_2)_2\text{SnI}_3$ ,  $\text{CH}_3\text{NH}_3\text{PbI}_3$ ,  $\text{HC}(\text{NH}_2)_2\text{PbI}_3$  and  $\text{CH}_3\text{NH}_3\text{Sn}_{1-x}\text{Pb}_x\text{I}_3$ , and studied the structure, morphology, phase transition and photoluminescence. In 2014, Kawano et al. [6] prepared three perovskites  $(\text{C}_4\text{H}_9\text{NH}_3)_2\text{PbBr}_4$ ,  $(\text{C}_6\text{H}_5\text{CH}_2\text{NH}_3)_2\text{PbBr}_4$  and  $(\text{C}_6\text{H}_5\text{C}_2\text{H}_4\text{NH}_3)_2\text{PbBr}_4$ , investigating the effects of organic moieties on luminescence properties of perovskite compounds. In 2015, Qin et al. [13] studied the performance of light-emitting diodes based on perovskite  $\text{CH}_3\text{NH}_3\text{PbBr}_3$ , and a high luminance up to  $1500 \text{ cd/m}^2$  was achieved. In 2018, Luo et al. [20] studied solar cells with the inverted planar heterojunction perovskite, yielding a PCE of 21% due to the elimination of nonradiative charge-carrier recombination. Droseros et al. [21] studied the photoluminescence of the perovskite  $\text{CH}_3\text{NH}_3\text{PbBr}_3$ , discovering the photoluminescence quantum yield (PLQY) increased with decreasing crystal size and explained the phenomenon.

Organic inorganic hybrid perovskites combine distinct properties of organic and inorganic components within a single molecular composite. The inorganic component forms the octahedral framework by ionic bonds, to provide good conductivity and carrier mobility. The organic component facilitates the self-assembly, enabling the materials to be deposited using a simple way. These properties can be easily controlled by changing the organic ammonium, inorganic metal or halide [22]. Research on perovskites is now focusing on solar cells and light-emitting diodes, however reports on the photoluminescent properties of the perovskites with the two-photon excitation are rarely seen. In this paper, the perovskites  $(\text{C}_6\text{H}_5\text{CH}_2\text{NH}_3)_2\text{PbBr}_4$  and  $(\text{C}_6\text{H}_5\text{CH}_2\text{NH}_3)_2\text{PbI}_4$  are synthesized by solvent evaporation. The laser power effect on the photoluminescence (PL) intensity and lifetime was investigated with femtosecond laser via the two-photon excitation.

## 2. Experimental Section

### 2.1. Synthesis of Organic Ammonium Salt

HBr and HI were added in the  $\text{C}_6\text{H}_5\text{CH}_2\text{NH}_2$  solution respectively. The mixtures were heated at  $50^\circ\text{C}$  and cooled at room temperature.  $\text{C}_6\text{H}_5\text{CH}_2\text{NH}_3\text{Br}$  and  $\text{C}_6\text{H}_5\text{CH}_2\text{NH}_3\text{I}$  were obtained and then heat treated.

### 2.2. Synthesis of Perovskite Crystal

$\text{C}_6\text{H}_5\text{CH}_2\text{NH}_3\text{Br}$  and  $\text{PbBr}_2$ ,  $\text{C}_6\text{H}_5\text{CH}_2\text{NH}_3\text{I}$  and  $\text{PbI}_2$  were then dissolved in *N,N*-dimethylformamide (DMF) in a molar ratio of 2:1 respectively. The mixtures were heated at  $50^\circ\text{C}$  and stirred for 1 h, then the perovskites  $(\text{C}_6\text{H}_5\text{CH}_2\text{NH}_3)_2\text{PbBr}_4$  and  $(\text{C}_6\text{H}_5\text{CH}_2\text{NH}_3)_2\text{PbI}_4$  were prepared by solvent evaporation. The products were washed with ethanol followed by heat treatment.

### 2.3. Synthesis of Perovskite Nanosheet

The perovskite crystals were ground into powders, which were used for XRD measurement. The perovskite powders were put in aqueous solution, ultrasonically processed, and then centrifuged. After a period of time, large quantities of perovskite nanosheets were obtained for TEM measurement. The chemical reaction equations involved in the experiment are as follows:



## 2.4. Characterization

The structure was analyzed by X-ray diffraction (Germany Bruker AXS, D8 Advance). The morphology was observed by transmission electron microscopy (Japan JEOL, JEM-2000) and scanning electron microscopy (Holland FEI, SEM 450). The absorption spectra were measured with UV-visible spectrometer (America PerkinElmer, Lambda 35). The optical measurements were performed using a commercial optical microscope system (Japan, Olympus IX73). A Ti:sapphire oscillator (China Atop Electronic Technology Co. Ltd., Vitara) was used for two-photon excitation. The laser beam was focused by an objective (Olympus, NA = 0.65) onto the samples. The reflected signal was collected by the same objective and then directed into a spectrometer (Andor 193i) for spectral measurement, or onto a CCD camera for imaging. The time correlated single photon count (TCSPC) system consisting of a PicoHarp 300 controller, a PDL 800-B reference and a SPDA-15 detector was used for the lifetime measurements. Figure 1 shows the optical path of the photoluminescence test system used in the experiment.

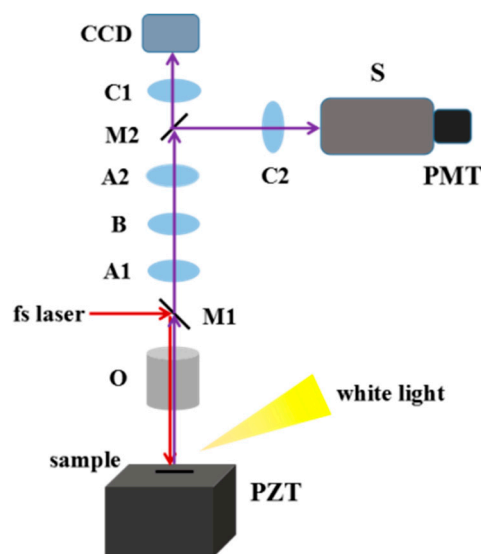


**Figure 1.** The experiment optical path of photoluminescence test system. PZT, piezoelectric ceramic transducer; O, objective; A, half-wave plate; B, polarizer; C, low pass filter; M, reflector; CCD, charge couple device; S, spectrometer; PMT, photomultiplier tube.

The experimental results can be fitted to a biexponential decay function:

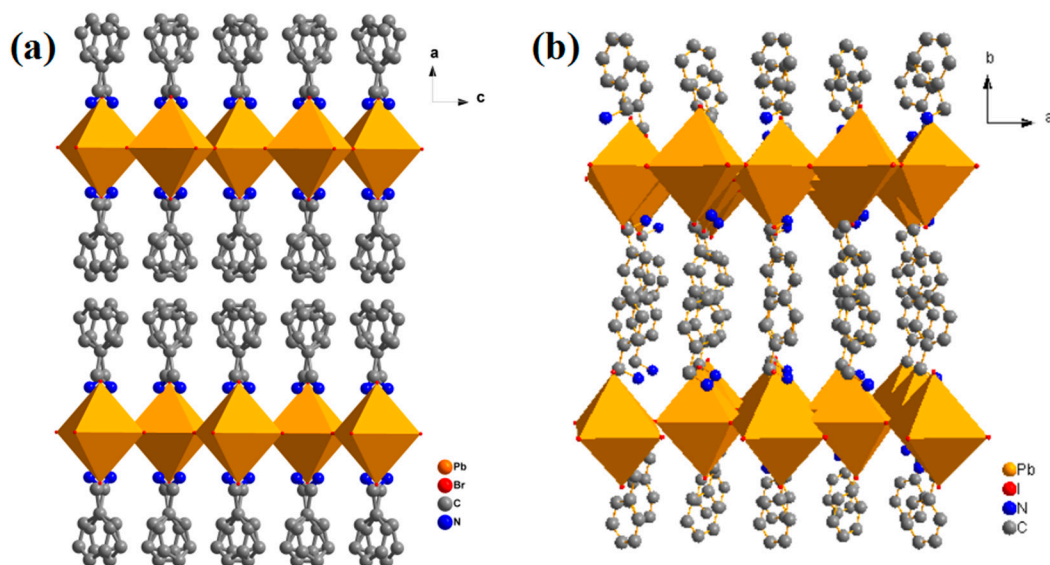
$$I = A_1 \exp(-t/\tau_1) + A_2 \exp(-t/\tau_2) \quad (5)$$

where  $\tau_1$  and  $\tau_2$  are the radiative and nonradiative decay lifetime, respectively.

## 3. Results and Discussion

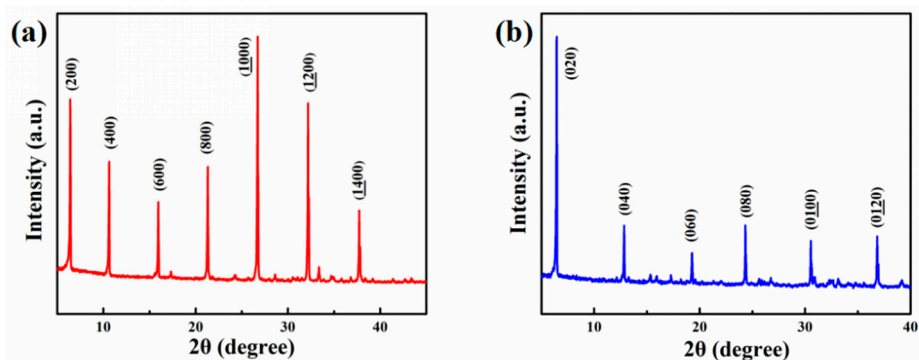
### 3.1. Structure Characterization

Figure 2a,b shows the crystal structure of the perovskites  $(C_6H_5CH_2NH_3)_2PbBr_4$  and  $(C_6H_5CH_2NH_3)_2PbI_4$ . The Pb atoms are six-coordinated by the halogen to form  $[PbX_6]$  octahedrons, which are corner-sharing to constitute three-dimensional frameworks. It can be observed that the perovskites  $(C_6H_5CH_2NH_3)_2PbBr_4$  and  $(C_6H_5CH_2NH_3)_2PbI_4$  exhibit the structure with alternating organic and inorganic layers. The growth directions of the layers are along the a axis and b axis, respectively. The lattice parameters of the perovskite  $(C_6H_5CH_2NH_3)_2PbBr_4$  and  $(C_6H_5CH_2NH_3)_2PbI_4$  are  $a = 3.3394$  nm,  $b = 0.8153$  nm,  $c = 0.8131$  nm and  $a = 0.8689$  nm,  $b = 2.878$  nm,  $c = 0.9162$  nm, which are consistent with reports in the literature [23].



**Figure 2.** The crystal structure of the perovskites (a)  $(\text{C}_6\text{H}_5\text{CH}_2\text{NH}_3)_2\text{PbBr}_4$ ; (b)  $(\text{C}_6\text{H}_5\text{CH}_2\text{NH}_3)_2\text{PbI}_4$ . The hydrogen atoms bonded to the carbon atoms are omitted for clarity.

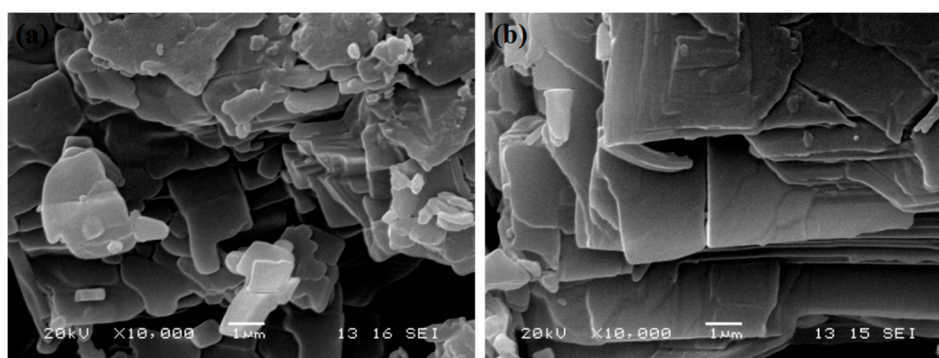
Figure 3a,b shows the XRD patterns of the perovskite powders  $(\text{C}_6\text{H}_5\text{CH}_2\text{NH}_3)_2\text{PbBr}_4$  and  $(\text{C}_6\text{H}_5\text{CH}_2\text{NH}_3)_2\text{PbI}_4$ . The diffraction peaks of the perovskite  $(\text{C}_6\text{H}_5\text{CH}_2\text{NH}_3)_2\text{PbBr}_4$  are located at  $6.41^\circ$ ,  $10.63^\circ$ ,  $15.96^\circ$ ,  $21.32^\circ$ ,  $26.72^\circ$ ,  $32.18^\circ$  and  $37.73^\circ$ , which correspond to the lattice plane  $(X00, X = 2, 4, 6, 8, \dots)$ . The diffraction peaks of the perovskite  $(\text{C}_6\text{H}_5\text{CH}_2\text{NH}_3)_2\text{PbI}_4$  are located at  $6.14^\circ$ ,  $12.29^\circ$ ,  $18.48^\circ$ ,  $24.73^\circ$ ,  $31.05^\circ$  and  $37.47^\circ$ , which are correspond to the lattice plane  $(0X0, X = 2, 4, 6, 8, \dots)$ . The calculated interlayer spacing of the perovskites  $(\text{C}_6\text{H}_5\text{CH}_2\text{NH}_3)_2\text{PbBr}_4$  and  $(\text{C}_6\text{H}_5\text{CH}_2\text{NH}_3)_2\text{PbI}_4$  are 1.44 nm and 1.68 nm, respectively, using the Bragg formula:  $2d\sin\theta = n\lambda$ . The experimental XRD patterns of the perovskites  $(\text{C}_6\text{H}_5\text{CH}_2\text{NH}_3)_2\text{PbBr}_4$  and  $(\text{C}_6\text{H}_5\text{CH}_2\text{NH}_3)_2\text{PbI}_4$  are consistent with calculated values, confirming there is no tri-halide perovskite or  $\text{PbX}_2$  phase [23]. All the patterns confirmed that the perovskites  $(\text{C}_6\text{H}_5\text{CH}_2\text{NH}_3)_2\text{PbBr}_4$  and  $(\text{C}_6\text{H}_5\text{CH}_2\text{NH}_3)_2\text{PbI}_4$  are well crystallized and oriented.



**Figure 3.** The XRD patterns of the perovskite powders (a)  $(\text{C}_6\text{H}_5\text{CH}_2\text{NH}_3)_2\text{PbBr}_4$ ; (b)  $(\text{C}_6\text{H}_5\text{CH}_2\text{NH}_3)_2\text{PbI}_4$ .

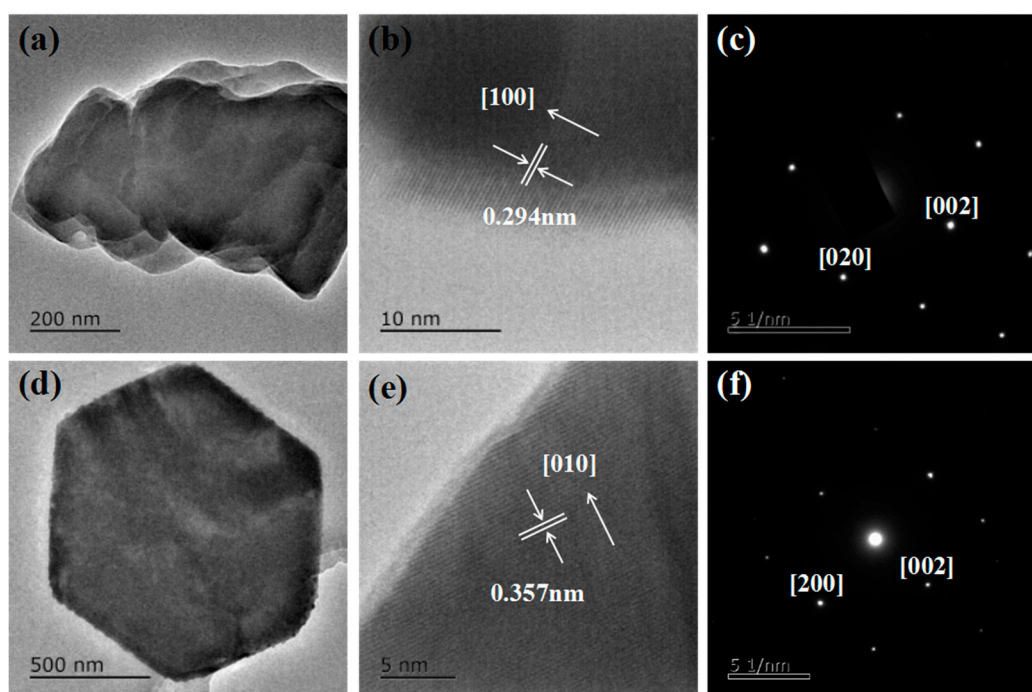
### 3.2. Morphology Characterization

Figure 4a,b shows the SEM images of the perovskites  $(\text{C}_6\text{H}_5\text{CH}_2\text{NH}_3)_2\text{PbBr}_4$  and  $(\text{C}_6\text{H}_5\text{CH}_2\text{NH}_3)_2\text{PbI}_4$ . The perovskite  $(\text{C}_6\text{H}_5\text{CH}_2\text{NH}_3)_2\text{PbBr}_4$  exhibits a layered stacking structure with grain size of 1–5  $\mu\text{m}$ , and the perovskite  $(\text{C}_6\text{H}_5\text{CH}_2\text{NH}_3)_2\text{PbI}_4$  also exhibits a layered stacking structure with grain size of 2–8  $\mu\text{m}$ . SEM images of the perovskites  $(\text{C}_6\text{H}_5\text{CH}_2\text{NH}_3)_2\text{PbBr}_4$  and  $(\text{C}_6\text{H}_5\text{CH}_2\text{NH}_3)_2\text{PbI}_4$  are consistent with those observed in the bright field TEM images.



**Figure 4.** SEM images of the perovskites (a)  $(\text{C}_6\text{H}_5\text{CH}_2\text{NH}_3)_2\text{PbBr}_4$ ; (b)  $(\text{C}_6\text{H}_5\text{CH}_2\text{NH}_3)_2\text{PbI}_4$ .

Figure 5a shows the bright field TEM images of the perovskite  $(\text{C}_6\text{H}_5\text{CH}_2\text{NH}_3)_2\text{PbBr}_4$  nanosheets. The perovskite  $(\text{C}_6\text{H}_5\text{CH}_2\text{NH}_3)_2\text{PbBr}_4$  displays a layered stacking structure with crystal geometry size of 600 nm. Figure 5b shows the HR-TEM images of the perovskite  $(\text{C}_6\text{H}_5\text{CH}_2\text{NH}_3)_2\text{PbBr}_4$  nanosheets. It shows that the lattice plane has the spacing distance of 0.294 nm, with the growth direction along [100]. The selected area electron diffraction (SAED) pattern of the perovskite  $(\text{C}_6\text{H}_5\text{CH}_2\text{NH}_3)_2\text{PbBr}_4$  nanosheets is shown in Figure 5c, indicating the orthorhombic phase, space group  $\text{Cmca}$ , with a growth direction along [100]. Figure 5d shows the bright field TEM images of the perovskite  $(\text{C}_6\text{H}_5\text{CH}_2\text{NH}_3)_2\text{PbI}_4$  nanosheets. The perovskite  $(\text{C}_6\text{H}_5\text{CH}_2\text{NH}_3)_2\text{PbI}_4$  displays a layered stacking structure with crystal geometry size of 1 μm. Figure 5e shows the HR-TEM images of the perovskite  $(\text{C}_6\text{H}_5\text{CH}_2\text{NH}_3)_2\text{PbI}_4$  nanosheets. It shows that the lattice plane has the spacing distance of 0.357 nm, with the growth direction along [010]. The SAED pattern of the perovskite  $(\text{C}_6\text{H}_5\text{CH}_2\text{NH}_3)_2\text{PbI}_4$  nanosheets is shown in Figure 5f, indicating the orthorhombic phase, space group  $\text{Pbca}$ , with a growth direction along [010].



**Figure 5.** (a) The bright field TEM images, (b) HR-TEM images and (c) Selected area electron diffraction (SAED) pattern of the perovskite  $(\text{C}_6\text{H}_5\text{CH}_2\text{NH}_3)_2\text{PbBr}_4$  nanosheets; (d) the bright field TEM images, (e) HR-TEM images and (f) SAED pattern of the perovskite  $(\text{C}_6\text{H}_5\text{CH}_2\text{NH}_3)_2\text{PbI}_4$  nanosheets.

### 3.3. Absorption Spectrum

Figure 6 shows the absorption spectrum of the perovskites  $(C_6H_5CH_2NH_3)_2PbBr_4$  (red curve) and  $(C_6H_5CH_2NH_3)_2PbI_4$  (blue curve). The absorption peaks are located at 392 nm (3.16 eV) and 516 nm (2.40 eV), which belong to the typical exciton absorption peaks. Organic inorganic hybrid perovskites have multiple quantum well structures with alternating organic and inorganic layers, therefore the excitons possess larger binding energy, and it is easy to generate exciton absorption due to quantum confinement effects.

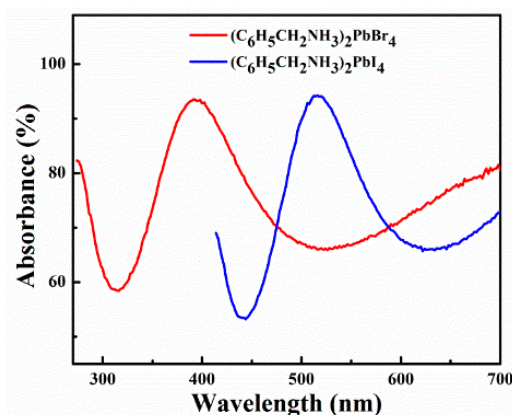
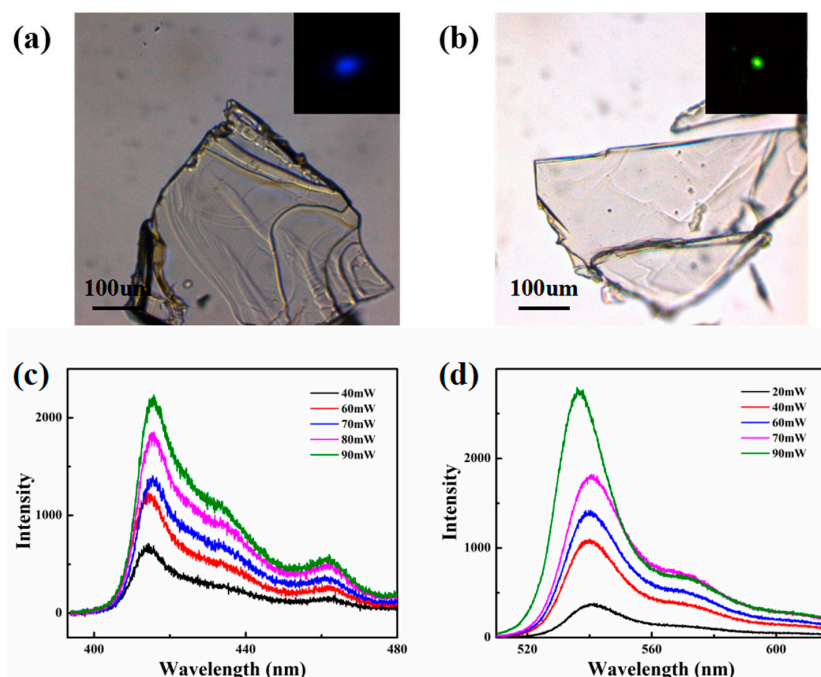


**Figure 6.** The absorption spectra of the perovskites  $(C_6H_5CH_2NH_3)_2PbBr_4$  (red curve) and  $(C_6H_5CH_2NH_3)_2PbI_4$  (blue curve).

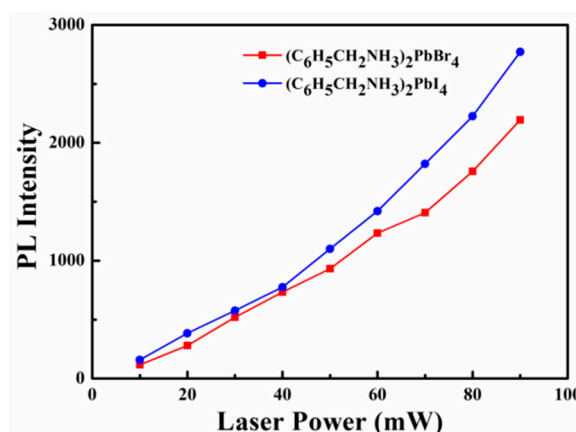
### 3.4. The Laser Power Effect on the PL Intensity

Figure 7a,b shows the bright field and dark field optical microscope images of the perovskites  $(C_6H_5CH_2NH_3)_2PbBr_4$  and  $(C_6H_5CH_2NH_3)_2PbI_4$ . It is possible to observe the regular and transparent crystal geometry of the perovskites  $(C_6H_5CH_2NH_3)_2PbBr_4$  and  $(C_6H_5CH_2NH_3)_2PbI_4$ , which emit blue and green photoluminescence under the 800 nm femtosecond laser. Figure 7c,d shows the two-photon PL spectrum of the perovskites  $(C_6H_5CH_2NH_3)_2PbBr_4$  and  $(C_6H_5CH_2NH_3)_2PbI_4$ . PL peaks are located at 415 nm (298 eV) and 540 nm (2.30 eV) respectively. PL intensity of the perovskite  $(C_6H_5CH_2NH_3)_2PbBr_4$  increases from 117 photon counts to 2195 photon counts when laser power increases from 10 mW to 100 mW. In contrast, PL intensity of the perovskite  $(C_6H_5CH_2NH_3)_2PbI_4$  increases from 158 photon counts to 2771 photon counts when laser power increases from 10 mW to 100 mW.

Figure 8 shows the laser power dependence of the PL intensity of the perovskites  $(C_6H_5CH_2NH_3)_2PbBr_4$  (red curve) and  $(C_6H_5CH_2NH_3)_2PbI_4$  (blue curve). It can be observed the PL intensity increases with increasing laser power. PL intensity of the perovskite  $(C_6H_5CH_2NH_3)_2PbBr_4$  is less than that of the perovskite  $(C_6H_5CH_2NH_3)_2PbI_4$  at the same laser power. The radius of a Br atom is less than that of an I atom, and the lattice volume of  $(C_6H_5CH_2NH_3)_2PbBr_4$  is less than that of  $(C_6H_5CH_2NH_3)_2PbI_4$ . Therefore the perovskite  $(C_6H_5CH_2NH_3)_2PbI_4$  has a larger Bohr radius and smaller exciton binding energy, so the excitons of the perovskite  $(C_6H_5CH_2NH_3)_2PbI_4$  will more easily separate and produce radiative recombination.



**Figure 7.** The bright field and dark field optical microscope images of the perovskites (a)  $(\text{C}_6\text{H}_5\text{CH}_2\text{NH}_3)_2\text{PbBr}_4$ ; (b)  $(\text{C}_6\text{H}_5\text{CH}_2\text{NH}_3)_2\text{PbI}_4$ ; the two-photon PL spectrum of the perovskites (c)  $(\text{C}_6\text{H}_5\text{CH}_2\text{NH}_3)_2\text{PbBr}_4$ ; (d)  $(\text{C}_6\text{H}_5\text{CH}_2\text{NH}_3)_2\text{PbI}_4$ .



**Figure 8.** Laser power dependence of the photoluminescence (PL) intensity of the perovskites  $(\text{C}_6\text{H}_5\text{CH}_2\text{NH}_3)_2\text{PbBr}_4$  (red curve) and  $(\text{C}_6\text{H}_5\text{CH}_2\text{NH}_3)_2\text{PbI}_4$  (blue curve).

### 3.5. The Laser Power Effect on the PL Lifetime

Figure 9a,b shows the PL lifetime of the perovskites  $(\text{C}_6\text{H}_5\text{CH}_2\text{NH}_3)_2\text{PbBr}_4$  and  $(\text{C}_6\text{H}_5\text{CH}_2\text{NH}_3)_2\text{PbI}_4$ . PL lifetime of the perovskite  $(\text{C}_6\text{H}_5\text{CH}_2\text{NH}_3)_2\text{PbBr}_4$  decreases from 0.75 ns to 0.50 ns when laser power increases from 10 mW to 100 mW. In contrast, PL lifetime of the perovskite  $(\text{C}_6\text{H}_5\text{CH}_2\text{NH}_3)_2\text{PbI}_4$  decreases from 0.67 ns to 0.46 ns when laser power increases from 10 mW to 100 mW. Figure 9c shows the laser power dependence of the PL intensity of the perovskites  $(\text{C}_6\text{H}_5\text{CH}_2\text{NH}_3)_2\text{PbBr}_4$  (red curve) and  $(\text{C}_6\text{H}_5\text{CH}_2\text{NH}_3)_2\text{PbI}_4$  (blue curve). It can be observed that the PL lifetime decreases with increasing laser power. PL lifetime of the perovskite  $(\text{C}_6\text{H}_5\text{CH}_2\text{NH}_3)_2\text{PbBr}_4$  is larger than that of the perovskite  $(\text{C}_6\text{H}_5\text{CH}_2\text{NH}_3)_2\text{PbI}_4$  at the same laser power. The internal quantum efficiency [6] is calculated as:

$$Q = \tau_{\text{nr}} / (\tau_{\text{r}} + \tau_{\text{nr}}) \quad (6)$$

where  $\tau_r$  and  $\tau_{nr}$  are the radiative and nonradiative decay lifetime respectively. According to Equation (6), the internal quantum efficiency of the perovskite  $(C_6H_5CH_2NH_3)_2PbBr_4$  varies from 81.48% to 90.91%, and the internal quantum efficiency of the perovskite  $(C_6H_5CH_2NH_3)_2PbI_4$  varies from 83.55% to 91.28%.

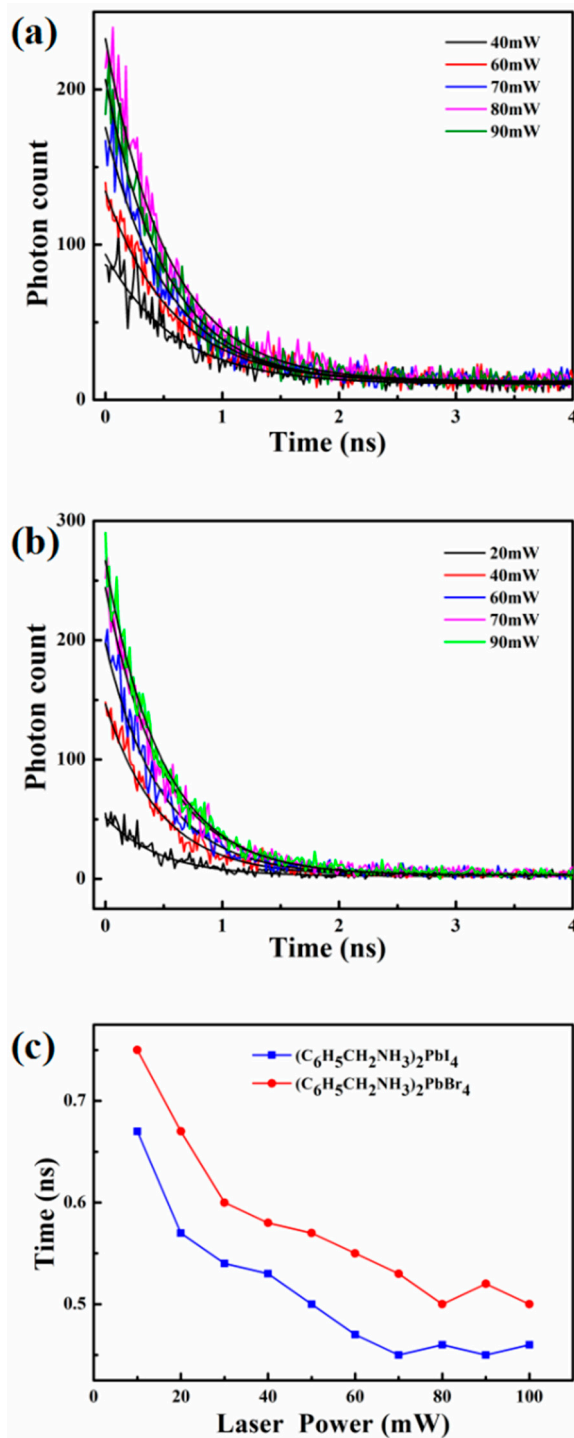


**Figure 9.** The PL lifetime of the perovskites (a)  $(C_6H_5CH_2NH_3)_2PbBr_4$ ; (b)  $(C_6H_5CH_2NH_3)_2PbI_4$ ; (c) laser power dependence of the PL lifetime of the perovskites  $(C_6H_5CH_2NH_3)_2PbBr_4$  (red curve) and  $(C_6H_5CH_2NH_3)_2PbI_4$  (blue curve).

The fluence-dependence of PL intensity and lifetime with laser power can be explained with the energy level diagram [24–26], which is shown in Figure 10. The perovskite molecules will absorb two

photons after the 800 nm laser excitation, promoting the electron transfer from VB to CB. Some electrons in CB will return to VB and produce exciton emission. Meanwhile, some electrons in CB will move to ESS by relaxation. The relaxation to ESS, or ESS recombination, can possess certain non-geminate recombination characteristics. This emission is a kind of non-geminate recombination, which is the intensity-dependent two-photon absorption cross-section [27]. When laser power increases, more electrons transfer from VB to CB, and move to ESS by relaxation after absorbing two photons. As a consequence, the carrier density increases and the emission is dominated by non-geminate recombination, which results in the increase of PL intensity and decrease of lifetime.

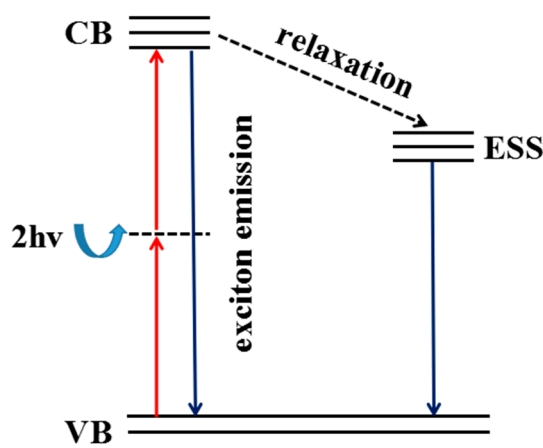


**Figure 10.** Energy level diagram of the perovskite molecule. VB, valence band; CB, conduction band; ESS, electron surface states.

#### 4. Conclusions

In this paper, we prepared the perovskites  $(\text{C}_6\text{H}_5\text{CH}_2\text{NH}_3)_2\text{PbBr}_4$  and  $(\text{C}_6\text{H}_5\text{CH}_2\text{NH}_3)_2\text{PbI}_4$  via solvent evaporation. The perovskites  $(\text{C}_6\text{H}_5\text{CH}_2\text{NH}_3)_2\text{PbBr}_4$  and  $(\text{C}_6\text{H}_5\text{CH}_2\text{NH}_3)_2\text{PbI}_4$  were well crystallized and oriented, and exhibited the layered structures with alternating organic and inorganic components. The absorption peaks were located at 392 nm (3.16 eV) and 516 nm (2.40 eV) respectively. PL intensity of the perovskite  $(\text{C}_6\text{H}_5\text{CH}_2\text{NH}_3)_2\text{PbBr}_4$  increased from 117 photon counts to 2195 photon counts, PLQY varied from 81.48% to 90.91%, and lifetime decreased from 0.75 ns to 0.50 ns when laser power increased from 10 mW to 100 mW. In contrast, PL intensity of the perovskite  $(\text{C}_6\text{H}_5\text{CH}_2\text{NH}_3)_2\text{PbI}_4$  increased from 158 photon counts to 2771 photon counts, PLQY varied from 83.55% to 91.28%, and lifetime decreased from 0.67 ns to 0.46 ns when laser power increased from 10 mW to 100 mW. The fluence-dependence of PL intensity and lifetime with laser power is mainly due to the non-geminate recombination. The photoluminescence properties of organic inorganic hybrid perovskites can be tuned to a wide range, which has important applications in the optoelectronic field.

**Author Contributions:** S.L. carried out the experiment and wrote the manuscript; F.L. helped in revising the manuscript; X.H., L.X., F.Y. and Y.L. helped in doing the experiment and analyzing the data.

**Funding:** This research was supported by the National Natural Science Foundation of China (Grant No. 11204222), the Natural Science Foundation of Hubei Province, China (Grant No. 2013CFB316, Grant No. 2014CFB793), the Postgraduate Education Innovation Fund, Wuhan Institute of Technology (No. CX2016106).

**Acknowledgments:** S.L. would like to thank for the support from Laboratory of Optical Information and Technology, Wuhan Institute of Technology; Wuhan National Laboratory for Optoelectronics, Huazhong University of Science and Technology.

**Conflicts of Interest:** The authors declare no conflict of interest.

## References

1. Egger, D.A.; Rappe, A.M.; Kronik, L. Hybrid Organic-Inorganic Perovskites on the Move. *Acc. Chem. Res.* **2016**, *49*, 573–581. [[CrossRef](#)] [[PubMed](#)]
2. Li, W.; Wang, Z.M.; Deschler, F.; Gao, S.; Friend, R.H.; Cheetham, A.K. Chemically diverse and multifunctional hybrid, organic–inorganic perovskites. *Nat. Rev. Mater.* **2017**, *2*, 16099. [[CrossRef](#)]
3. Kim, T.W.; Uchida, S.; Matsushita, T.; Cojocaru, L.; Jono, R.; Kimura, K.; Matsubara, D.; Shirai, M.; Ito, K.; Matsumoto, H.; et al. Self-Organized Superlattice and Phase Coexistence inside Thin Film Organometal Halide Perovskite. *Adv. Mater.* **2018**, *30*, 1705230. [[CrossRef](#)] [[PubMed](#)]
4. Gui, D.; Ji, L.J.; Muhammad, A.; Li, W.; Cai, W.Z.; Li, Y.C.; Li, X.D.; Wu, X.; Lu, P.X. Jahn-Teller Effect on Framework Flexibility of Hybrid Organic-inorganic Perovskites. *Phys. Chem. Lett.* **2018**, *9*, 751–7554. [[CrossRef](#)] [[PubMed](#)]
5. Dong, L.Y.; Sun, S.J.; Deng, Z.Y.; Li, W.; Wei, F.X.; Qi, Y.J.; Li, Y.C.; Li, X.D.; Lu, P.X.; Ramamurty, U. Elastic properties and thermal expansion of lead-free halide double perovskite Cs<sub>2</sub>AgBiBr<sub>6</sub>. *Comput. Mater. Sci.* **2018**, *141*, 49–58. [[CrossRef](#)]
6. Kawano, N.; Koshimizu, M.; Sun, Y.; Yahaha, N.; Fujimoto, Y.; Yanagida, T.; Asai, K. Effects of Organic Moieties on Luminescence Properties of Organic–Inorganic Layered Perovskite-Type Compounds. *J. Phys. Chem. C* **2014**, *118*, 9101–9106. [[CrossRef](#)]
7. Tanaka, K.; Kondo, T. Bandgap and exciton binding energies in lead-iodide-based natural quantum-well crystals. *Sci. Technol. Adv. Mater.* **2003**, *4*, 599–604. [[CrossRef](#)]
8. Zhang, S.J.; Audebert, P.; Wei, Y.; Choueiry, A.A.; Lanty, G.; Bréhier, A.; Galmiche, L.; Clavier, G.; Boissière, C.; Lauret, J.S.; Deleporte, E. Preparations and Characterizations of Luminescent Two Dimensional Organic-inorganic Perovskite Semiconductors. *Materials* **2010**, *3*, 3385–3406. [[CrossRef](#)]
9. Khadka, D.B.; Shirai, Y.; Yanagida, M.; Masuda, T.; Miyano, K. Enhancement in efficiency and optoelectronic quality of perovskite thin films annealed in MAI vapor. *Sustain. Energy Fuels* **2017**, *1*, 755–766. [[CrossRef](#)]
10. Xu, L.T.; Li, F.; Wei, L.; Zhou, J.X.; Liu, S. Design of Surface Plasmon Nanolaser Based on MoS<sub>2</sub>. *Appl. Sci.* **2018**, *8*, 2110. [[CrossRef](#)]
11. Xu, L.T.; Li, F.; Liu, S.; Yao, F.Q.; Liu, Y.H. Low Threshold Plasmonic Nanolaser Based on Graphene. *Appl. Sci.* **2018**, *8*, 2186. [[CrossRef](#)]
12. Fang, H.H.; Raissa, R.; Aguye, M.A.; Adjokatsé, S.; Blake, G.R.; Even, J.; Loi, M.A. Photophysics of Organic–Inorganic Hybrid Lead Iodide Perovskite Single Crystals. *Adv. Funct. Mater.* **2015**, *25*, 2346. [[CrossRef](#)]
13. Qin, X.; Dong, H.L.; Hu, W.P. Green light-emitting diode from bromine based organic inorganic halide perovskite. *Sci. China Mater.* **2015**, *58*, 186–191. [[CrossRef](#)]
14. Khadka, D.B.; Shirai, Y.; Yanagida, M.; Ryan, J.W.; Miyano, K. Exploring the effects of interfacial carrier transport layers on device performance and optoelectronic properties of planar perovskite solar cells. *J. Mater. Chem. C* **2017**, *5*, 8819–8827. [[CrossRef](#)]
15. Bandiello, E.; Avila, J.; Gil-Escrig, L.; Tekelenburg, E.; Sessolo, M.; Bolink, H.J. Influence of mobile ions on the electroluminescence characteristics of methylammonium lead iodide perovskite diodes. *J. Mater. Chem. A.* **2016**, *4*, 18614–18620. [[CrossRef](#)]
16. Stoumpos, C.C.; Malliakas, C.D.; Peters, J.A.; Liu, Z.F.; Sebastian, M.; Im, J.; Chasapis, T.C.; Wibowo, A.C.; Chung, D.Y.; Freeman, A.J.; et al. Crystal Growth of the Perovskite Semiconductor CsPbBr<sub>3</sub>: A New Material for High-Energy Radiation Detection. *Cryst. Growth Des.* **2013**, *13*, 2722–2727. [[CrossRef](#)]
17. Kojima, A.; Teshima, K.; Shirai, Y.; Miyasaka, T. Organometal halide perovskites as visible-light-sensitizers for photovoltaic cells. *J. Am. Chem. Soc.* **2009**, *131*, 6050–6051. [[CrossRef](#)] [[PubMed](#)]
18. Zheng, Y.Y.; Deng, H.T.; Wan, J.; Li, C.R. Bandgap energy tuning and photoelectrical properties of self-assembly quantum well structure in organic-inorganic hybrid perovskites. *Acta Phys. Sin.* **2011**, *60*, 646–652.
19. Stoumpos, C.C.; Malliakas, C.D.; Kanatzidis, M.G. Semiconducting Tin and Lead Iodide Perovskites with Organic Cations: Phase Transitions, High Mobilities, and Near-Infrared Photoluminescent Properties. *Inorg. Chem.* **2013**, *52*, 9019–9038. [[CrossRef](#)] [[PubMed](#)]
20. Luo, D.; Yang, W.; Wang, Z.; Sadhanala, A.; Hu, Q.; Su, R. Enhanced photovoltage for inverted planar heterojunction perovskite solar cells. *Science* **2018**, *360*, 1442–1446. [[CrossRef](#)] [[PubMed](#)]

21. Droseros, N.; Longo, G.; Brauer, J.C.; Sessolo, M.; Bolink, H.J.; Banerji, N. Origin of the Enhanced Photoluminescence Quantum Yield in MAPbBr<sub>3</sub> Perovskite with Reduced Crystal Size. *ACS Energy Lett.* **2018**, *3*, 1458–1466. [[CrossRef](#)]
22. Dou, S.Y.; Yan, L.T.; Liu, Y.C.; Du, G.; Zhou, P. Preparation and performance of organic–inorganic halide perovskites. *J. Mater. Sci.* **2013**, *24*, 4862–4867. [[CrossRef](#)]
23. Liao, W.Q.; Zhang, Y.; Hu, C.L.; Mao, J.G.; Ye, H.Y.; Li, P.F.; Huang, S.D.; Xiong, R.G. A lead-halide perovskite molecular ferroelectric semiconductor. *Nat. Commun.* **2015**, *6*, 7338. [[CrossRef](#)] [[PubMed](#)]
24. Li, F.; He, Z.C.; Li, M.Y.; Zhang, J.P.; Han, J.B.; Lu, P.X. Photoinduced energy transfer in a CdTe quantum dot–copper phthalocyanine system via two-photon excitation. *Mater. Lett.* **2014**, *132*, 263–266. [[CrossRef](#)]
25. Li, M.Y.; Li, F.; He, Z.C.; Zhang, J.P.; Han, J.B.; Lu, P.X. Two-Photon-Excited Fluorescence Resonance Energy Transfer in an Aqueous System of CdTe Quantum Dots and Rhodamine B. *J. Appl. Phys.* **2014**, *116*, 233106. [[CrossRef](#)]
26. Li, F.; He, Z.C.; Li, M.Y.; Lu, P.X. Three-Photon Absorption of Copper Phthalocyanine Solution by Femtosecond Z-scan Technique. *Mater. Lett.* **2013**, *111*, 81–84. [[CrossRef](#)]
27. Liu, W.W.; Li, X.H.; Song, Y.L.; Zhang, C.; Han, X.B.; Long, H.; Wang, B.; Wang, K.; Lu, P.X. Cooperative Enhancement of Two-Photon-Absorption-Induced Photoluminescence from a 2D Perovskite-Microsphere Hybrid Dielectric Structure. *Adv. Funct. Mater.* **2018**, *28*, 1707550. [[CrossRef](#)]



© 2018 by the authors. Licensee MDPI, Basel, Switzerland. This article is an open access article distributed under the terms and conditions of the Creative Commons Attribution (CC BY) license (<http://creativecommons.org/licenses/by/4.0/>).